catalysts

Article

Experimental Clarification of the RWGS Reaction Effect in H_2O/CO_2 SOEC Co-Electrolysis Conditions

Evangelia Ioannidou [1,2], Stylianos Neophytides [1] and Dimitrios K. Niakolas [1,*]

1 Foundation for Research and Technology, Institute of Chemical Engineering Sciences (FORTH/ICE-HT), Patras, GR-26504, Greece; eioannidou@iceht.forth.gr (E.I.); neoph@iceht.forth.gr (S.N.)
2 Department of Chemical Engineering, University of Patras, GR-56504, Greece
* Correspondence: niakolas@iceht.forth.gr

Received: 31 December 2018; Accepted: 29 January 2019; Published: 2 February 2019

Abstract: In the present investigation, modified X-Ni/GDC electrodes (where X = Au, Mo, and Fe) are studied, in the form of half-electrolyte supported cells, for their performance in the RWGS through catalytic-kinetic measurements. The samples were tested at open circuit potential conditions in order to elucidate their catalytic activity towards the production of CO (r_{co}), which is one of the products of the H_2O/CO_2 co-electrolysis reaction. Physicochemical characterization is also presented, in which the samples were examined in the form of powders and as half cells with BET, H_2-TPR, Air-TPO and TGA re-oxidation measurements in the presence of H_2O. In brief, it was found that the rate of the produced CO (r_{co}) increases by increasing the operating temperature and the partial pressure of H_2 in the reaction mixture. In addition, the first results revealed that Fe and Mo modification enhances the catalytic production of CO, since the 2wt% Fe-Ni/GDC and 3wt% Mo-Ni/GDC electrodes were proven to perform better compared to the other samples, in the whole studied temperature range (800–900 °C), reaching thermodynamic equilibrium. Furthermore, carbon formation was not detected.

Keywords: SOECs; RWGS reaction kinetics; Au–Mo–Fe-Ni/GDC electrodes; high temperature H_2O/CO_2 co-electrolysis

1. Introduction

Solid oxide electrolysis is a contemporary process for CO_2 capture/recycling, which is proven as an attractive method to provide CO_2 neutral synthetic hydrocarbon fuels. In particular, co-electrolysis of H_2O and CO_2 in a solid oxide electrolysis cell (SOEC) yields synthesis gas (CO + H_2), which in turn can be used towards the formation of various types of synthetic fuels [1–3] by applying the Fischer-Tropsch process. According to thermodynamics, SOECs offer benefits for endothermic reactions, such as H_2O and/or CO_2 electrolysis at temperatures >700 °C, because a larger part of the required electrical energy can be substituted by thermal energy [4,5]. In addition, high temperature can lead to a significant decrease in the internal resistance of the cell and acceleration of the electrode reaction processes due to fast reaction kinetics [4–7].

H_2O/CO_2 Co-electrolysis is a much more complex process compared to pure steam or CO_2 electrolysis. This is because three reactions take place simultaneously, namely H_2O electrolysis, CO_2 electrolysis, and the catalytic Reverse Water Gas Shift reaction (RWGS). More specifically, at the cathode of SOECs, two electrochemical reactions take place in parallel at the triple phase boundaries, i.e., H_2O and CO_2 electrochemical reductions. The oxygen ions (O^{2-}), produced by these reactions, are moved to the anode, through an oxygen ion-conducting electrolyte (Yttria-Stabilized Zirconia − YSZ), where oxygen (O_2) gas is formed [8,9]:

$$\text{Cathode:} \quad H_2O + 2e^- \rightarrow H_2 + O^{2-} \quad \Delta H_{800\,^\circ C} = 151.8\ \text{kJ/mol} \tag{1}$$

$$CO_2 + 2e^- \rightarrow CO + O^{2-} \quad \Delta H_{800\,^\circ C} = 185.9\ kJ/mol \tag{2}$$

$$\text{Anode:} \qquad O^{2-} \rightarrow \frac{1}{2}\,O_2 + 2e^- \tag{3}$$

Besides the electrolysis reactions mentioned above, the reversible water gas shift (RWGS) catalytic reaction also occurs at the cathode with the co-existence of CO_2 and H_2O:

$$\text{Cathode:} \qquad H_2 + CO_2 \rightarrow H_2O + CO \quad \Delta H_{800\,^\circ C} = 36.8\ kJ/mol \tag{4}$$

It thus appears that CO can be produced either electrocatalytically by the reduction of CO_2 or catalytically via the RWGS reaction. Questionable conclusions have been proposed in the literature about the role of the RWGS reaction for CO production. Some studies mention that CO is mainly produced electrocatalytically and RWGS has a small participation [10–15], while other studies mention that CO is absolutely produced catalytically via the RWGS reaction [16,17]. However, it has not been shown conclusively to which degree the RWGS is responsible for CO production in an SOEC.

Specifically, Mogensen and co-researchers found that the performance of co-electrolysis on an Ni/YSZ cathode varied between the highest pure H_2O electrolysis and the lowest CO_2 electrolysis, being much closer to the prior process [13,14]. This implies the significant contribution of the RWGS reaction in the H_2O/CO_2 SOEC co-electrolysis process and also confirms the co-existence of CO_2 electrolysis. The above conclusion was supported by recently published results on computational modelling of the direct and indirect (with electro-generated H_2) reduction of CO_2 [18,19]. The direction of the Water Gas Shift (WGS) reaction could be forward or backward, depending on the operating conditions, indicating that at high temperatures (>838 °C), CO was produced electrochemically and the WGS was shifted in reverse towards H_2 and CO_2.

In contrast, Yue and Irvine [20] suggested that the RWGS reaction did not contribute critically in catalysing H_2O/CO_2 co-electrolysis on s (La,Sr)(Cr,Mn)O_3 (LSCM) perovskite based cathode. The LSCM cathode displayed higher catalytic activity for pure CO_2 electrolysis than pure H_2O electrolysis, and the performance for H_2O/CO_2 co-electrolysis was much closer to pure CO_2 electrolysis.

On the other hand, Bae et al., Hartvigsen et al., Kee et al., and Zhao et al. considered that CO production on Ni-based cathodes was mainly from the RWGS reaction, whereas the electrochemical processes are dominated by H_2O electrolysis with identical performances for H_2O electrolysis and H_2O/CO_2 co-electrolysis [16,17,21].

According to the above mentioned reports, until now, no agreement has been reached regarding the role of the RWGS reaction in the production of CO. As a result, it is crucial to quantify the degree of CO formation for each reaction. The discrepancies regarding the CO production route can be affected both by the structural characteristics of the electrode/catalyst (specific surface area, reducibility and re-oxidation behaviour, porosity, particle size, ionic and electronic conductivity), but also by the operating conditions (gas composition, temperature, etc.) [9,22]. As reported by Li's study [10], the heterogeneous thermochemical reactions occur at the external surface of the cathode and they are 20–100 times faster than the electrochemical reactions, which occur close to the electrolyte at the three phase boundaries. Furthermore, structural modifications of the cathode could enhance mass transport and promote CO production through the catalytic RWGS reaction, resulting in H_2O/CO_2 co-electrolysis performance close to that of H_2O electrolysis.

The majority of studies on high temperature H_2O/CO_2 co-electrolysis utilize Ni-containing ceramic cathodes with YSZ and Gadolinia-Doped Ceria (GDC), similarly to the case of H_2O electrolysis [10–14]. Ni-based materials indeed are cheap and exhibit porous structure, high electronic conductivity, appropriate catalytic activity, and a similar Thermal Expansion Coefficient (TEC) with the electrolyte. Consequently, they could act as excellent SOECs cathodes for H_2O/CO_2 co-electrolysis [7,22–26].

However, SOECs comprising Ni-based cathodes face some critical degradation issues, which are more pronounced with an increasing current density [3,12,14,27–33]. The main reasons for degradation have been reported to be microstructural changes that take place after prolonged co-electrolysis, resulting in passivation and blocking of the Three-Phase Boundaries (TPB) area [12,13,28,30,31,33,34]. Post-mortem microscopy investigations in the Ni/YSZ electrode have shown irreversible damages of the electrode's microstructure, such as loss of Ni-YSZ contact, decomposition of YSZ, Ni grain growth, loss of Ni percolation (loss of Ni–Ni contact), and even migration of Ni from the fuel electrode [28,30,31,33]. Taking into account the above, it is critical to develop alternative cathode materials for H_2O/CO_2 co-electrolysis with improved structural properties.

Previous studies reported that the electrocatalytic efficiency of SOECs can be improved by alloying transition metals with the state of the art (SoA) Ni catalyst [35–39]. Modification by means of alloying may be a promising strategy to promote the catalytic activity due to ligand and strain effects that change the electronic structure [40] of the active element. Recent studies focused on the Ni–Co alloy with Sm-doped ceria (Ni–Co/SDC) as an alternative material, with enhanced performance for H_2O electrolysis in SOECs [36]. Specifically, the addition of Co increased the intrinsic catalytic activity of pure Ni and simultaneously expanded the active reaction region [36,41]. Other reports have shown that an Ni–Fe bimetallic cathode, mixed with $Ba_{0.6}La_{0.4}CoO_3$ on $La_{0.9}Sr_{0.1}Ga_{0.8}Mg_{0.2}O_3$ (LSGM) electrolyte, improved the electrochemical performance of the electrode for H_2O electrolysis [38] and CO_2 electrolysis [39], due to prevention of Ni aggregation. Furthermore, the enhanced performance of the Ni–Fe formulations could be attributed to the increased stability and improved catalytic activity, due to the addition of Fe, as this was concluded by combining experimental results with theoretical Density Functional Theory (DFT) calculations [41].

Our research group have studied the effect of Au and/or Mo doping on the physicochemical and catalytic properties of Ni/GDC for the reactions of catalytic CH_4 dissociation and methane steam reforming [23,42–45] in the presence of H_2 and H_2S impurities. These modifications resulted in SOFC fuel electrodes with high sulfur and carbon tolerance as well as with improved electrocatalytic activity. Regarding the doping level of Au and Mo, the amount of 3wt% was indicated as an appropriate loading for achieving the most promising results under the examined SOFC conditions. Recently, the 3wt% Au-Ni/GDC electrode was tested under SOEC conditions for the H_2O electrolysis process and exhibited improved electrocatalytic performance compared to Ni/GDC [46]. The enhanced performance of the Au-doped cathode was attributed to the creation of a surface Ni–Au solid solution, which causes weaker interplay of absorbed H_2O_{ads} and O_{ads} species with the modified cathode. The result is a durable and resistant electrode to surface oxidation with an improved "three phase boundaries" area, especially at temperatures higher than 800 °C [46].

The presented investigation deals with modified X-Ni/GDC electrodes (where X = Au, Mo, Fe), in the form of half-Electrolyte Supported Cells (ESCs), for their performance in the RWGS through catalytic-kinetic measurements. Ni/GDC, 3wt% Au-Ni/GDC, 3wt% Mo-Ni/GDC, 3wt% Au–3wt% Mo-Ni/GDC, and 2wt% Fe-Ni/GDC modified cathodes were tested at Open Circuit Potential (OCP) conditions to elucidate their catalytic activity towards the production of CO (r_{co}), which is one of the products from the H_2O/CO_2 co-electrolysis reaction. The latter approach is considered as an attempt to create a reference profile for the catalytic performance of the candidate electrodes, by applying the same $H_2O/CO_2/H_2$ feed conditions as those under the co-electrolysis operational mode. The samples, both in the form of powders and as half cells, were physicochemically characterized, including specific redox stability measurements in the presence of H_2O.

2. Results and Discussion

2.1. Physicochemical Characterization

2.1.1. Specific Surface Area Values of Au–Mo–Fe-Modified Powders

The specific surface area values (SSA) for the modified-NiO/GDC samples, calcined in air at 600 and 1100 °C, as well as after reduction with H_2 at 850 °C, are presented in Table 1.

The first remark is that all samples exhibit quite similar and low SSA values, which decrease further by increasing the calcination temperature from 600 °C to 1100 °C and after H_2 reduction at

850 °C. Furthermore, Mo and Au–Mo modification slightly decrease the SSA of Ni/GDC, while the addition of Fe causes a significant increase in the SSA values up to approximately 70%. Taking into account the generally low values and the ±0.2 m^2 g^{-1} accuracy limits of the measurements, it can be concluded that the reduced Mo and Au–Mo-Ni/GDC powders have similar SSAs with Ni/GDC. On the other hand, the 70% increase in the SSA of the Fe modified sample can be primarily ascribed to the formation of FeO_x species, in the oxidized form of the sample, which inhibit the decrease of SSA during reduction.

Table 1. BET Specific Surface Area (SSA_{BET}) of commercial NiO/GDC, and X-modified NiO/GDC samples (where X = Au, Mo, and Fe). The measurements were performed on powders, calcined at 600 °C, 1100 °C, and after H_2-reduction at 850 °C. Error/accuracy of SSA_{BET} = ±0.2 m^2 g^{-1}.

Sample Powder	**SSA_{BET} (m^2 g^{-1})**		
	T = 600 °C, (oxidized)	**T = 1100 °C, (oxidized)**	**After H_2-reduction at T = 850 °C**
NiO/GDC	5.3	2.9	2.0
3Au-NiO/GDC	5.4	2.7	2.1
3Mo-NiO/GDC	5.0	2.2	1.7
3Au–3Mo-NiO/GDC	5.1	2.4	1.8
2Fe-NiO/GDC	8.8	4.0	3.4

2.1.2. H_2 Reducibility and air Re-Oxidation Behaviour of Au–Mo–Fe-Modified Powders

Temperature Programmed Reduction followed by Oxidation (H_2-TPR, Air-TPO) measurements were performed, in order to investigate the reducibility and re-oxidation behavior of the prepared composite powders, as well as the existence of possible bulk effects due to the modification with Au, Mo, and Fe. The corresponding H_2-TPR and Air-TPO TGA profiles of modified-NiO/GDC samples, calcined at 1100 °C, are presented in Figure 1.

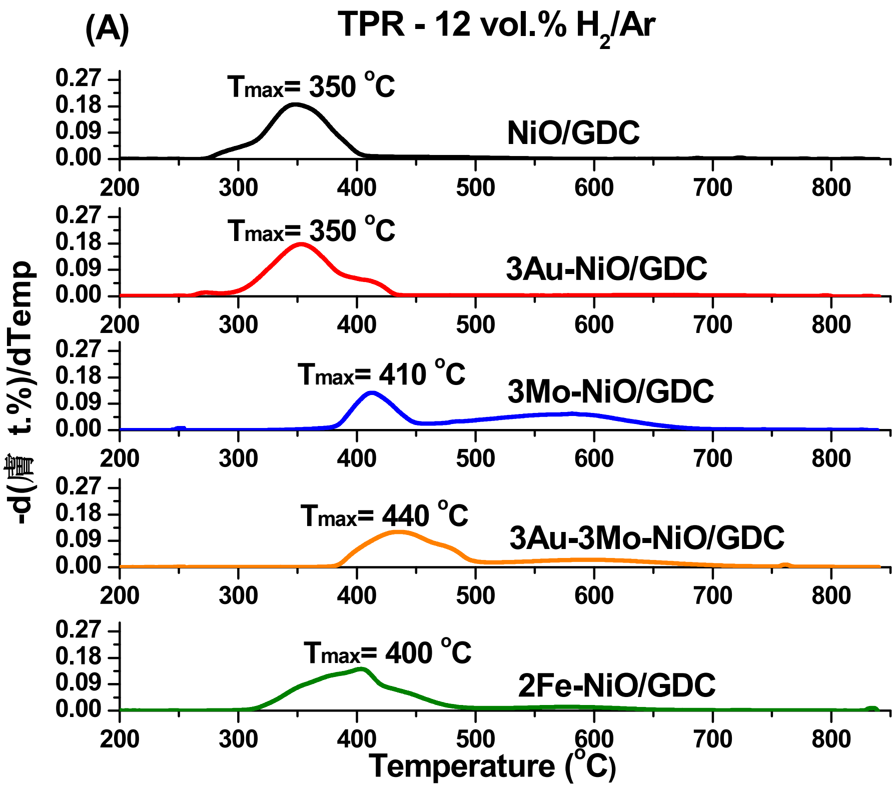

Figure 1. *Cont.*

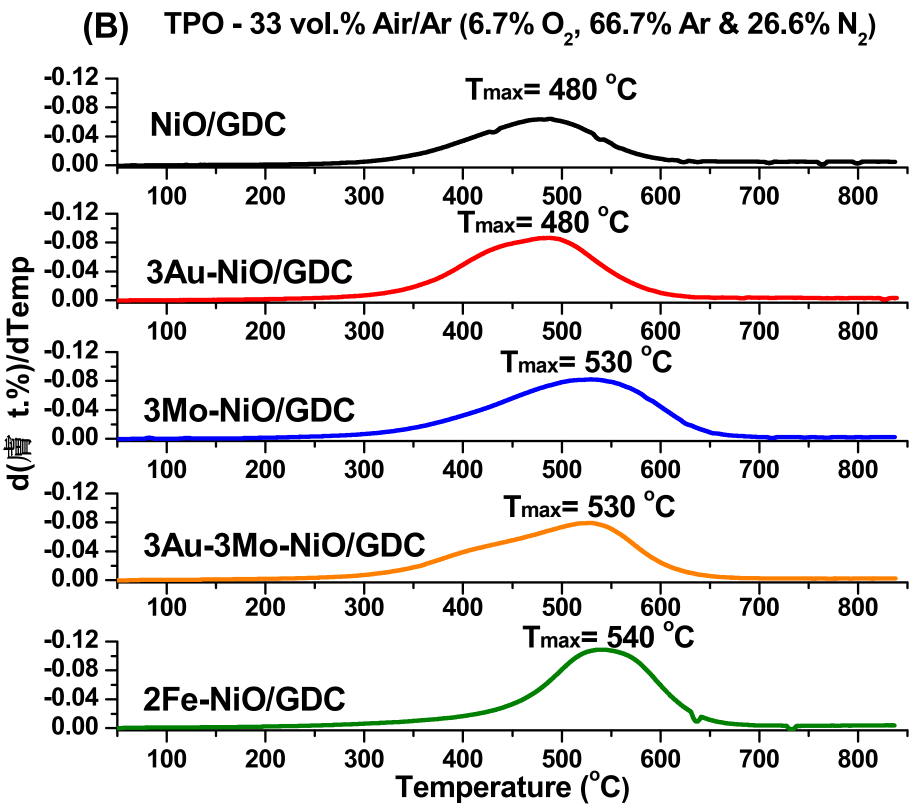

Figure 1. TGA (**A**) H_2-TPR (12 vol.% H_2/Ar), and (**B**) O_2-TPO (33 vol.% air) profiles of X-modified NiO/GDC samples (where X= Au, Mo, and Fe). The measurements were performed on powders, calcined at 1100 °C. F_{total} = 60 cm^3/min (STP conditions: 0 °C, 1 atm).

H_2-TPR and air-TPO measurements showed different reduction and oxidation behavior in each of the examined modified samples. In particular, two main reduction peaks (Figure 1A) and one oxidation peak (Figure 1B) are mainly observed, which can be attributed to the reduction of NiO species to Ni and the reverse [42,47]. Moreover, the presence of Au does not seem to affect significantly the reduction of NiO. On the other hand, MoO_3 and, to a certain extent, Fe inhibit the NiO reduction, implying a stronger Ni–O bond. The inhibition effect of MoO_3 is also observed in the case of the ternary 3Au–3Mo-NiO/GDC sample and indicates a bulk interaction between Ni–Au–Mo, which has been thoroughly investigated in previous studies [23,42,43]. In particular, the second broad peak ("shoulder") at 580 °C, which is observed for the 3Mo-NiO/GDC and 3Au–3Mo-NiO/GDC samples, may be associated with the reduction of MoO_3 species, which are reduced at higher temperatures in the range of 600–770 °C [42,47]. The presence of Fe seems to affect the main reduction peak of NiO, in a similar way as MoO_3, suggesting the possible formation of a solid solution between Ni and Fe. The latter observation is currently under further clarification.

Upon re-oxidation of the samples, the unmodified Ni/GDC as well as the Au modified sample are oxidized practically at the same temperature with a similar TPO profile. The reduced state of the Fe, Mo-, and Au–Mo- modified samples proved to be more resistant to re-oxidation in 33 vol.% air/Ar (6.7 vol.% O_2/Ar), since they had to reach higher temperature for complete re-oxidation.

2.1.3. H_2O Re-Oxidation Profiles of Au-Mo-Fe–Modified Powders

Isothermal-TGA measurements, under 15.5 vol.% H_2O/Ar conditions, were carried out at 650 °C, 700 °C, 750 °C, and 800 °C and the results are depicted in Figures 2 and 3. These measurements investigate the activity of the powders for the H_2O dissociation reaction and their concomitant re-oxidation rate. H_2O acts as an oxidative agent and interacts with the Ni atoms on the surface of each sample towards H_2 and NiO [reaction (5)] [46].

$$H_2O + Ni \rightarrow H_2 + NiO \quad (5)$$

Thereafter, there is a progressive diffusion of the absorbed oxygen species (O_{ads}) from the surface in the bulk phase of the sample, which is oxidized further [46,48–50]. Figure 2 depicts the H_2O re-oxidation profiles, as an increase of the weight (Δwt%), of the pre-reduced Ni/GDC, 3wt% Au-Ni/GDC, 3wt% Mo-Ni/GDC, 3wt% Au–3wt% Mo-Ni/GDC, and 2wt% Fe-Ni/GDC samples in the temperature range between 650–800 °C.

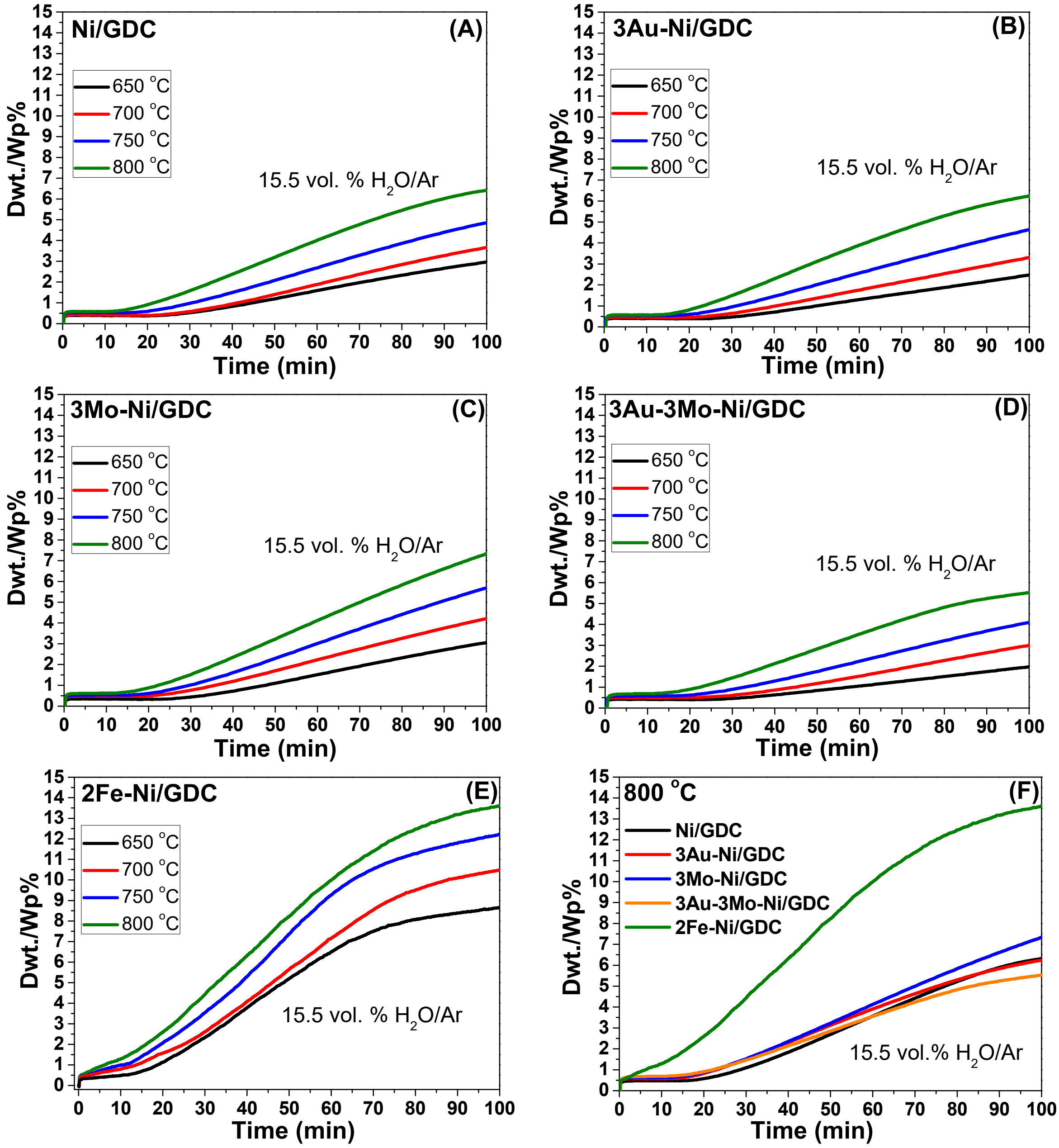

Figure 2. Isothermal TG analysis of the pre-reduced, (**A**) Ni/GDC, (**B**) 3wt% Au-Ni/GDC, (**C**) 3wt% Mo-Ni/GDC, (**D**) 3wt% Au–3wt% Mo-Ni/GDC, and (**E**) 2wt% Fe-Ni/GDC samples in the temperature range between 650–800 °C. (**F**) Comparative TG profiles of the samples at 800 °C. Feed Conditions: 15.5 vol.% H_2O/Ar, F_{total} = 100 cm^3/min (STP conditions: 0 °C, 1 atm).

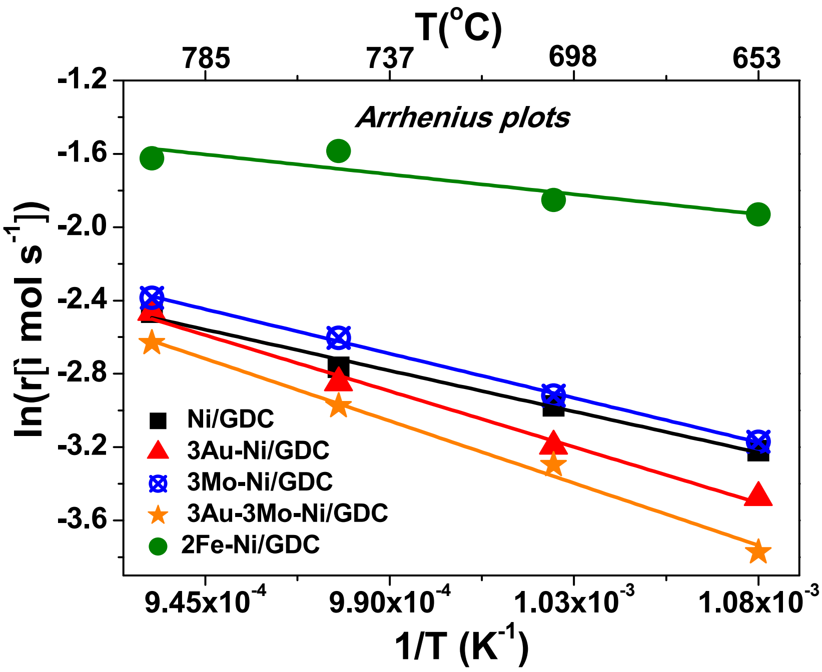

Figure 3. Arrhenius plots of the H_2O re-oxidation rate (resulting from the slope of the isothermal TG profiles in Figure 2) for: Ni/GDC, 3wt% Au-Ni/GDC, 3wt% Mo-Ni/GDC, 3wt% Au–3wt% Mo-Ni/GDC, and 2wt% Fe-Ni/GDC Feed Conditions: 15.5 vol.% H_2O/Ar, F_{total} = 110 cm^3/min (STP conditions: 0 °C, 1 atm).

The re-oxidation profiles of the samples in Figure 2 can be separated in three sections [46]. The first section corresponds to the initial sharp increase in weight and is ascribed [46] to the complete, bulk, re-oxidation of the partially reduced CeO_2 in GDC and specifically of Ce^{3+} to Ce^{4+}. The second section occurs during the following 12–25 min of the reaction, where the samples, except for 2Fe-Ni/GDC, keep their reduced state without any changes in their weight. This step is associated [46] to the dissociation of bulk NiH species, which are formed during the prior reduction period, and maintains the samples reduction. NiH dissociation is considered as an activated process, because by decreasing the operating temperature from 800 °C to 650 °C, the specific "delay" period increases from 12 min to 25 min. The first two sections are quite similar for the pre-reduced powders, with identical low SSA values (Table 1). On the other hand, the initial re-oxidation behavior, in the first section, of the pre-reduced 2Fe-Ni/GDC is more intense, indicating the strong effect of H_2O.

In the third section of the TG profiles, further re-oxidation takes place [reaction (5)] and the main discrepancies are detected among the samples. In the range of 650–800 °C, the ternary 3Au–3Mo-Ni/GDC sample is the most tolerant in bulk re-oxidation by H_2O, while the binary 2Fe-Ni/GDC sample is the least tolerant. The decrease in temperature (800 → 650 °C) leads to inhibition of the bulk re-oxidation, as observed by the reduced slopes in the TG profiles, whereas the trend among the samples does not change. The high tolerance of the 3Au–3Mo-Ni/GDC sample against bulk re-oxidation by H_2O is attributed to the synergistic interaction of nickel with gold and molybdenum [23,42].

The slope on the linear part of the third section in the TG curves represents the intrinsic dissociation rate of H_2O and correspondingly the re-oxidation rate of Ni atoms on each sample [reaction (5)] [46]. Figure 3 depicts the Arrhenius plots of the oxidation rates of the samples, which were calculated from the slopes on the linear parts of the TG profiles (Figure 2). The Arrhenius plots (Figure 3) show that the binary 2Fe-Ni/GDC sample has the highest H_2O re-oxidation rates, while the ternary 3Au–3Mo-Ni/GDC has the lowest. This is further confirmed by the calculated apparent activation energies ($E_{a,ap}$), which are defined from the Arrhenius plots and are reported in Table 2.

Table 2. Apparent activation energies (kJ mol^{-1}) for the dissociation of H_2O on commercial Ni/GDC [46], and modified Ni/GDC samples. The values correspond to the slopes of the Arrhenius plots in Figure 3.

Sample Powder	$E_{a, app}$ (kJ mol^{-1})
Ni/GDC [46]	41
3Au-Ni/GDC [46]	56
3Mo-Ni/GDC	45
3Au–3Mo-Ni/GDC	63
2Fe-Ni/GDC	20

The calculated values verify that the binary 2Fe-Ni/GDC sample exhibits the lowest $E_{a,ap}$ (20 kJ/mol) for the catalytic dissociation of H_2O, whereas the ternary 3Au–3Mo-Ni/GDC sample exhibits the highest $E_{a,ap}$ (63 kJ/mol). The above behavior can be interpreted by the fact that Ni-Fe interaction reinforces the bond of H_2O_{ads}, resulting in a higher re-oxidation rate (lower $E_{a,ap}$). On the other hand, following the same interpretation, Ni–Au–Mo interaction weakens the bond of H_2O_{ads}, resulting in a lower re-oxidation rate (higher $E_{a,ap}$) [46].

The calculated $E_{a,ap}$ values are in good agreement with our previous study [46] and other studies [51–53] in the literature, which focus on theoretical investigations. The binary 2Fe-Ni/GDC sample is the most active for the thermochemical dissociation of H_2O and is less resistant against bulk re-oxidation. On the contrary, the ternary 3Au–3Mo-Ni/GDC sample exhibits the lowest activity for the thermochemical dissociation of H_2O and the highest tolerance against bulk re-oxidation.

Taking into account the above, H_2O, apart from being the main reactant of the co-electrolysis process, is also considered as a potential poisoning agent of the electrode. This means that the bonding strength of the adsorbed oxygen species, which result from H_2O decomposition, may induce the re-oxidation of the electrode and finally the deactivation of the sample [46,53]. The H_2O poisoning effect in electrolysis and co-electrolysis processes can also be correlated to the CH_4 poisoning effect in SOFC applications, where degradation is enhanced by the strong adsorption bond of CH_4 on the Ni surface [23,42–45,54,55]. Thus, the stronger binding of the adsorbed oxygen species, which result from the catalytic dissociation of H_2O_{ads}, can similarly cause a poisoning effect on the Ni surface, leading to faster re-oxidation and finally deactivation of the sample [46,53]. According to Besenbacher et al. [56], the surface solid solution between Au and Ni induces significant modifications in the electronic properties of Ni (Fermi level, work function, and d-band center) and affects the bonding strength of the adsorbed species on the surface of the sample.

In this respect, the Au- and Au–Mo- doping of Ni should shift the d-band center to lower energies, with respect to the Fermi level of nickel, thus inhibiting the interaction and the dissociation of H_2O. Therefore, the 3Au-Ni/GDC and 3Au–3Mo-Ni/GDC samples are suggested to be the least active samples for the dissociation of H_2O, having the highest $E_{a,app}$ and consequently the lowest binding energies for both H_2O and O_{ads}. The binary 2Fe-Ni/GDC is suggested to be the most active sample for the dissociation of H_2O, with the lowest $E_{a,app}$, resulting in O_{ads} species with the highest binding energy and the potential to cause faster re-oxidation/poisoning of the electrode [46,53] during SOEC operation.

2.2. Catalytic-Kinetic Measurements of the RWGS Reaction

All the prepared samples, in the form of half-electrolyte supported cells, were tested at Open Circuit Potential (OCP) conditions to elucidate their catalytic activity towards the production of CO, which is one of the products from the H_2O/CO_2 co-electrolysis reaction. Furthermore, the effect of the modification (type of dopant: Au, Mo, Fe) on the catalytic activity for the production of CO, through the RWGS reaction, was also investigated. The latter approach is considered as an attempt to create a reference profile for the catalytic performance of the candidate electrodes, under the same experimental conditions as in co-electrolysis (including the presence of current collector). This is an important step, because it will provide detailed experimental feedback on the possible contribution of the RWGS reaction to the production of CO and the extent of this contribution to the electrochemical reduction of CO_2, during the co-electrolysis mode.

In regards to the "homogenous" catalytic production of CO, the rate was found to be negligible, in the range of $r_{co, homogenous}$ = 0.05 μmol/s, for a fuel feed comprising 30 vol.% He − 24.5 vol.% H_2O − 24.5 vol.% CO_2 − 21 vol.% H_2. Concerning the current collector, Ni-mesh shows some catalytic activity for the production of CO (r_{CO}), which increases by increasing the operating temperature and the partial pressure of H_2. However, comparative r_{CO} measurements (see Figure S1 in Supplementary Material) of an Ni/GDC electrode with and without the presence of Ni mesh as the current collector, as well as of the bare Ni mesh, suggest that there is no direct catalytic correlation/contribution of the Ni mesh to the activity of the electrocatalysts. This is mainly explained by the fact that Ni/GDC is a porous electrocatalyst with SSA_{BET} and thus with more active sites, compared to the metallic nickel mesh, which does not possess similar properties. Consequently, from the point where they co-exist as the electrode and current collector, the catalytic activity is mainly attributed to the electrocatalyst.

Figure 4 presents the comparison of the produced r_{CO} for the Ni/GDC and for modified-Ni/GDC electrodes, under three different H_2O-CO_2-H_2 mixtures. The corresponding %CO_2 conversions are depicted in Figure 5. The values are low enough to be considered in the differential region, apart from the case of 2Fe-Ni/GDC in the reaction mixture (A), which is relatively high. The % conversion of CO_2 was calculated by the following formula:

$$CO_2 \text{ conversion } (\%) = \frac{F_{CO}^{out}}{F_{CO_2}^{in}} \cdot 100 \tag{6}$$

where: F_{CO}^{out} and $F_{CO_2}^{in}$ correspond to the rate (μmol/s) of the produced CO and of the introduced CO_2 in the reactants feed, respectively.

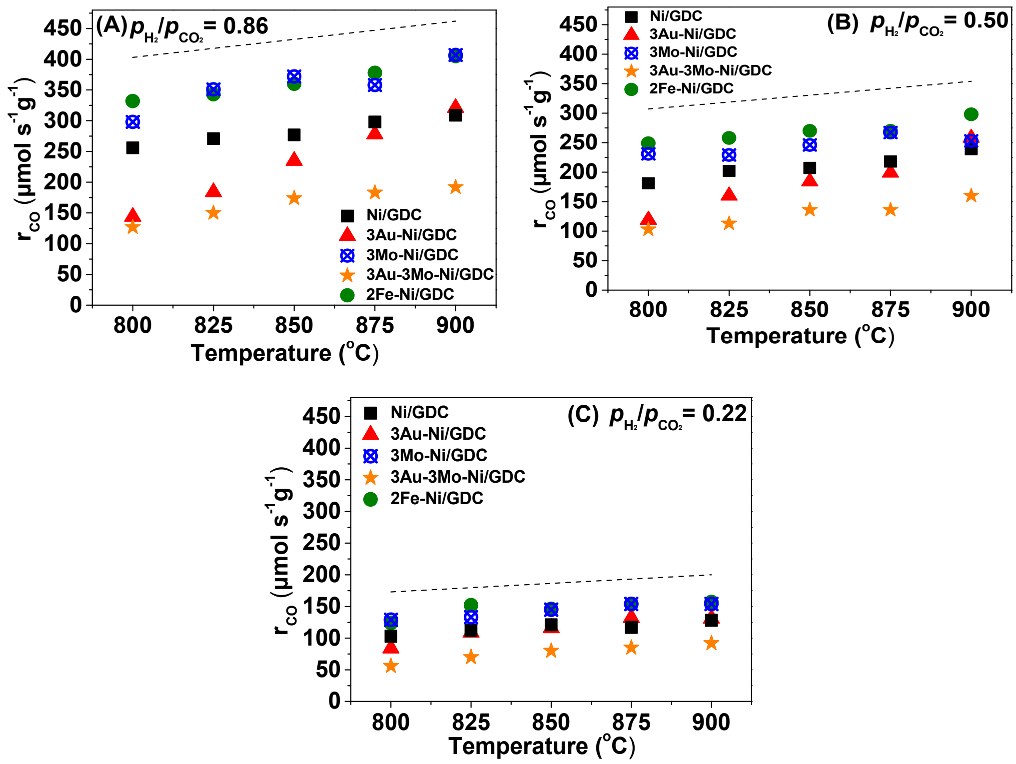

Figure 4. CO production rates (μmol s^{-1} g^{-1}) on ESCs comprising: Ni/GDC, 3Au-Ni/GDC, 3Mo-Ni/GDC, 3Au–3Mo-Ni/GDC, and 2Fe-Ni/GDC, as fuel electrodes, in the range of 800–900 °C under three different mixtures: (**A**) 24.5% H_2O − 24.5% CO_2 − 21% H_2 (P_{H2}/P_{CO_2} = 0.86), (**B**) 28% H_2O − 28% CO_2 − 14% H_2 (P_{H2}/P_{CO_2} = 0.50), and (**C**) 31.5% H_2O − 31.5% CO_2 − 7% H_2 (P_{H2}/P_{CO_2} = 0.22). Dilution of He: 30 vol.% and F_{total} = 140 cm^3/min (STP conditions: 0 °C, 1 atm) in all cases. The dash line (– –) corresponds to the r_{CO} values in thermodynamic equilibrium. All studied electrodes have similar loading in the range of 10–12 mg/cm^2.

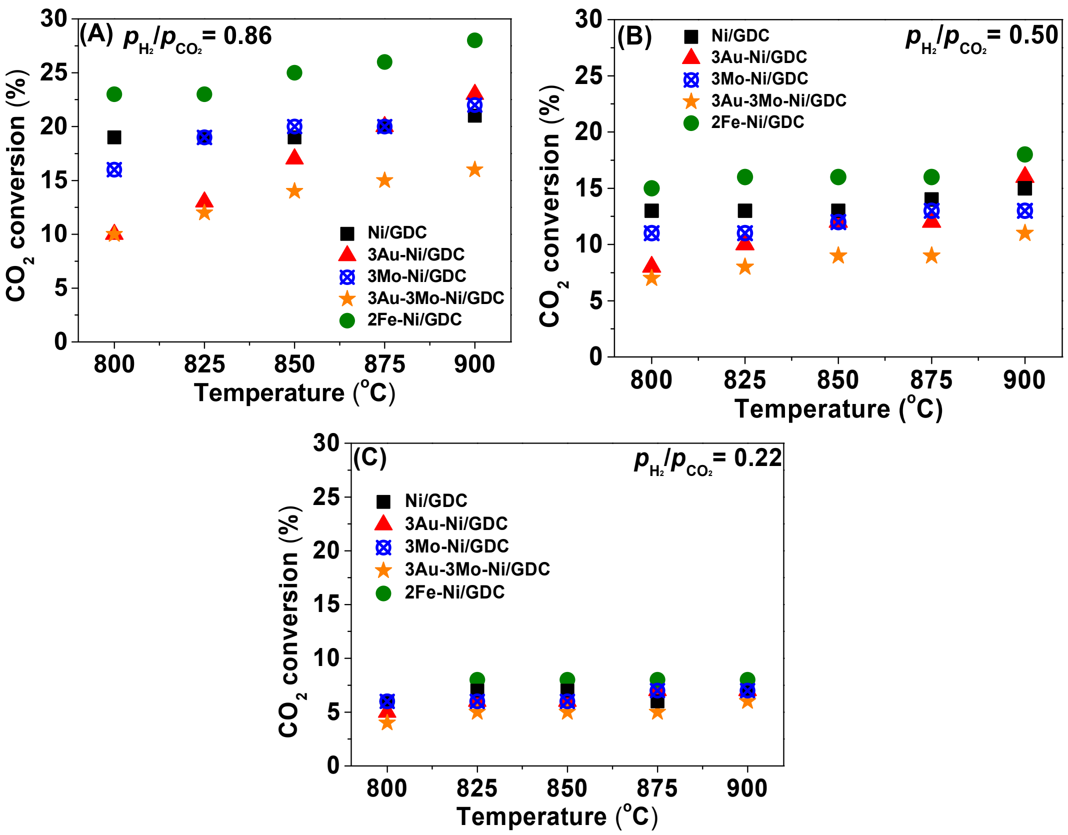

Figure 5. The corresponding $\%CO_2$ conversions of ESCs comprising: Ni/GDC, 3Au-Ni/GDC, 3Mo-Ni/GDC, 3Au–3Mo-Ni/GDC, and 2Fe-Ni/GDC, as fuel electrodes, in the range of 800–900 °C under three different mixtures: (**A**) 24.5% H_2O − 24.5% CO_2 − 21% H_2 (P_{H2}/P_{CO_2} = 0.86), (**B**) 28% H_2O − 28% CO_2 − 14% H_2 (P_{H2}/P_{CO_2} = 0.50), and (**C**) 31.5% H_2O − 31.5% CO_2 − 7% H_2 (P_{H2}/P_{CO_2} = 0.22). Dilution of He: 30 vol.% and F_{total} = 140 cm^3/min (at STP conditions: 0 °C, 1 atm) in all cases. All studied electrodes have similar loading in the range of 10–12 mg/cm^2.

It is shown (Figures 4 and 5) that 2Fe-Ni/GDC and 3Mo-Ni/GDC have the highest catalytic activity of the examined electrodes for the RWGS reaction. In fact, 2Fe-Ni/GDC is the most active in terms of the produced CO. The above performance is observed for all applied fuel feeds (P_{H2}/P_{CO_2} = 0.86, 0.50 and 0.22), whereas it is enhanced by increasing (i) the operating temperature and (ii) the partial pressure of H_2 in the fuel feed. The enhanced catalytic performance of the Fe-modified sample, can be primarily ascribed to the possible stronger adsorption and consequent catalytic dissociation of CO_2 on the active sites of the catalyst. This first conclusion is going to be further examined with specific CO_2 Temperature Programmed Desorption (TPD) measurements.

Another noteworthy remark is that the produced CO rates were compared to the thermodynamic equilibrium rates (dash line in Figure 4) for the three different H_2O-CO_2-H_2 reaction mixtures. The equilibrium rates were calculated by using the equilibrium constant (K_{eq}) formula that is reported in [57,58]. It was found (Figure 4) that Ni/GDC, the binary Au-, and the ternary Au–Mo- modified samples exhibit CO production rates, which are lower than the thermodynamic equilibrium for all the examined reaction conditions. The performances of 2Fe-Ni/GDC and 3Mo-Ni/GDC are closer to the equilibrium, but cannot be considered as thermodynamically limited.

The results from the measurements in Figure 4 can also be presented as Arrhenius plots, depicted in Figure 6, where the derived apparent activation energies ($E_{a,\,app}$) for the production of CO and consequently for the RWGS reaction are listed in Table 3.

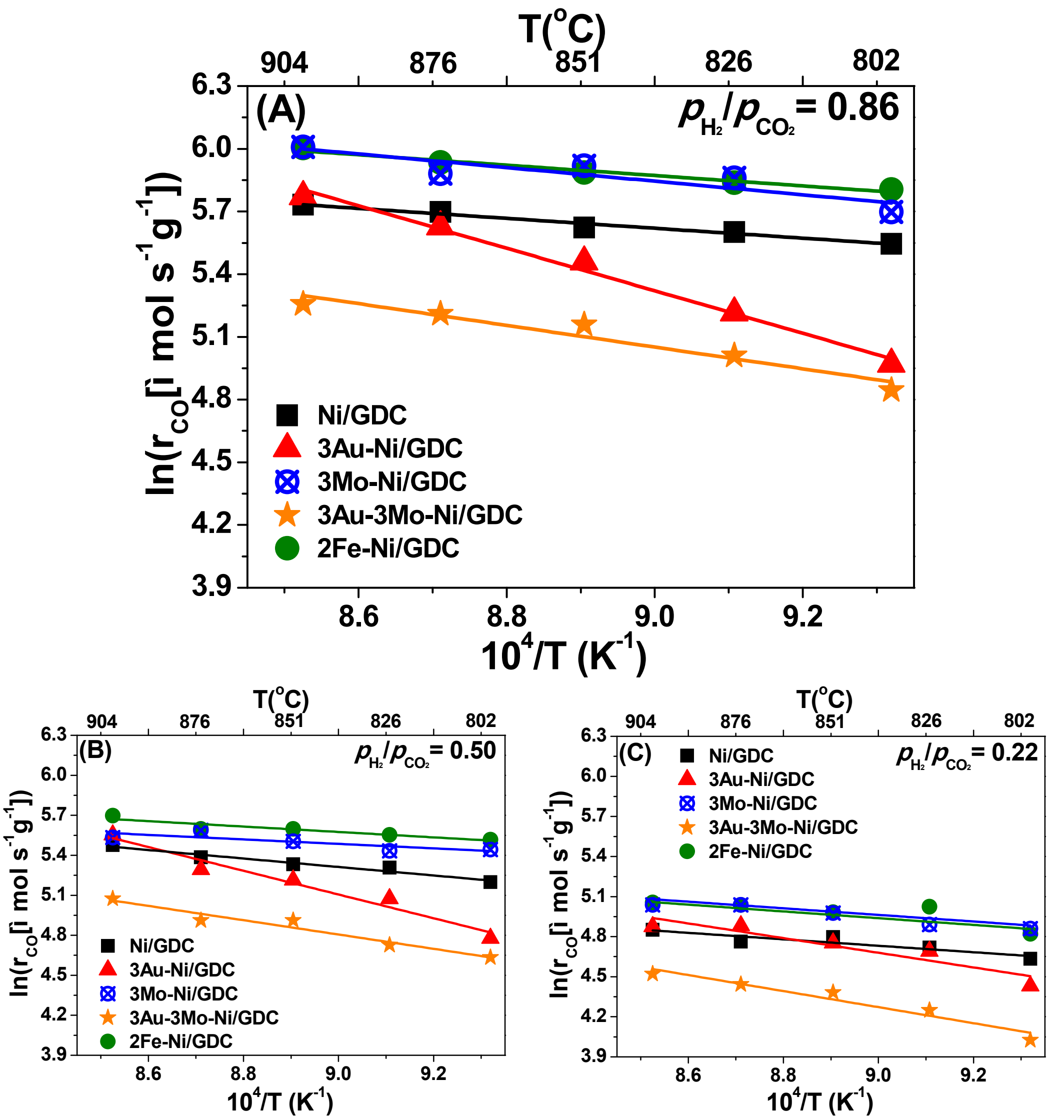

Figure 6. Arrhenius plots of the CO production rates (μmol s^{-1} g^{-1}) on ESCs comprising: Ni/GDC, 3Au-Ni/GDC, 3Mo-Ni/GDC, 3Au–3Mo-Ni/GDC, and 2Fe-Ni/GDC, in the range of 800–900 °C, under three different mixtures: (**A**) 24.5% H_2O − 24.5% CO_2 − 21% H_2 (P_{H2}/P_{CO_2} = 0.86), (**B**) 28% H_2O − 28% CO_2 − 14% H_2 (P_{H2}/P_{CO_2} = 0.50), and (**C**) 31.5% H_2O − 31.5% CO_2 − 7% H_2 (P_{H2}/P_{CO_2} = 0.22). Dilution of He: 30 vol.% and F_{total} = 140 cm^3/min (at STP conditions: 0 °C, 1 atm) in all cases.

Table 3. Apparent activation energies ($E_{a,app}$, kJ/mol) for the RWGS reaction on ESCs for three different mixtures: (**A**) 24.5% H_2O − 24.5% CO_2 − 21% H_2 (P_{H2}/P_{CO_2} = 0.86), (**B**) 28% H_2O − 28% CO_2 − 14% H_2 (P_{H2}/P_{CO_2} = 0.50), and (**C**) 31.5% H_2O − 31.5% CO_2 − 7% H_2 (P_{H2}/P_{CO_2} = 0.22).

Sample	**$E_{a,\ apparent}$ (kJ mol^{-1}) and A^* ($\mu mol\ s^{-1}\ g^{-1}$), per reaction mixture**					
	P_{H2}/P_{CO_2} = 0.86		**P_{H2}/P_{CO_2} = 0.50**		**P_{H2}/P_{CO_2} = 0.22**	
Ni/GDC	**20**	*2.3×10^3*	**22**	*3.6×10^3*	**20**	*1.0×10^3*
3Au-Ni/GDC	**85**	*1.9×10^6*	**74**	*5.0×10^5*	**46**	*1.5×10^4*
3Mo-Ni/GDC	**27**	*6.5×10^3*	**14**	*1.1×10^3*	**21**	*1.4×10^3*
3Au–3Mo-Ni/GDC	**43**	*1.7×10^4*	**45**	*1.5×10^4*	**50**	*1.6×10^4*
2Fe-Ni/GDC	**21**	*3.3×10^3*	**19**	*1.6×10^3*	**21**	*1.3×10^3*

*A: The pre-exponential factor in the Arrhenius equation, r = A$\cdot$exp$(-\frac{E_{a,app}}{R\cdot T})$.

The Arrhenius plots and the calculated $E_{a, app}$ show that 2Fe-Ni/GDC, 3Mo-Ni/GDC, and Ni/GDC have practically the same and the lowest $E_{a, app}$. However, the Fe- and Mo- modified samples exhibit higher pre-exponential factors, compared to Ni/GDC, which explains the higher production rates of CO. 3Au-Ni/GDC shows overall the highest $E_{a, app}$, which is an additional indication for its worst catalytic activity. Finally, the ternary 3Au–3Mo-Ni/GDC sample shows an apparent activation energy, which lies between that for 2Fe-Ni/GDC and 3Au-Ni/GDC. However, the catalytic activity of the ternary sample is the lowest, due to the lower pre-exponential factor compared to the binary Au-modified sample. According to the knowledge of the authors, there are no literature data available for experimentally measured $E_{a, app}$, for similar samples and reaction conditions. The so far available data come from theoretical investigations and there is a recent study from Cho et al. [41], who performed DFT calculations to evaluate the ability of various transition metals to increase the activity of Ni for the H_2O/CO_2 co-electrolysis. In particular, they computed the activation energies of specific elementary reaction steps and in the case of the RWGS on Ni(111), the E_a was found to be approximately 46 kJ/mole, which is very close to the values that were experimentally calculated in the present study.

The effect of H_2 partial pressure on the catalytic rate of CO production is further verified in Figure 7 for all samples at 900 °C and 800 °C. The 2Fe-Ni/GDC sample is the most active and 3Au–3Mo-Ni/GDC the least one. The 3Au-Ni/GDC catalyst at 900 °C shows similar performance with that of Ni/GDC. In addition, by decreasing the temperature at 800 °C, the catalytic activity of 3Au-Ni/GDC exhibits the highest reduction. This is apparent from the significant decrease in the slope of the corresponding curve (Figure 7) from 800 °C to 900 °C and can be further explained from the calculated $E_{a, app}$ (Table 3), which is the highest from all samples. Finally, the kinetic behavior of all samples suggests that the production rate of CO exhibits a positive order dependence on the partial pressure of H_2.

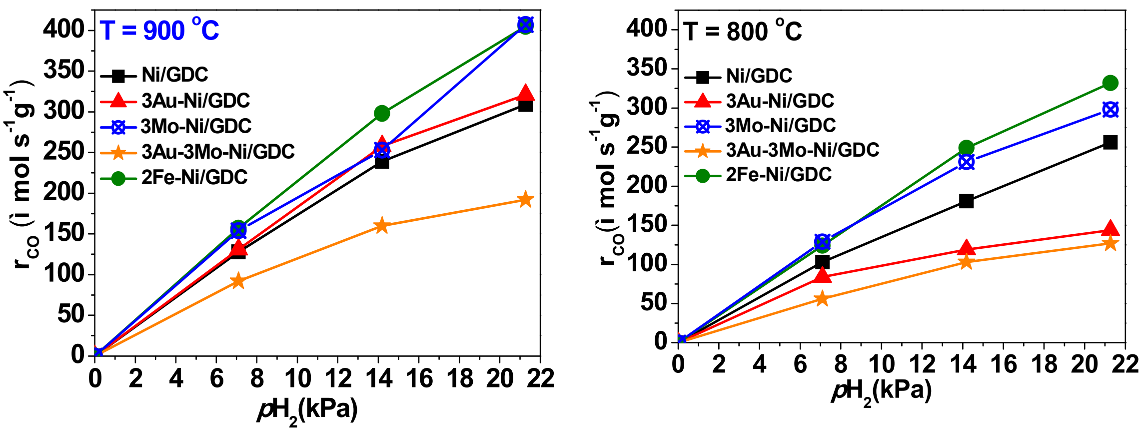

Figure 7. Steady state effect of the H_2 partial pressure (pH_2, kPa) on the CO production rates (μmol s^{-1} g^{-1}) on ESCs comprising: Ni/GDC, 3Au-Ni/GDC, 3Mo-Ni/GDC, 3Au–3Mo-Ni/GDC, and 2Fe-Ni/GDC, for 900 °C and 800 °C. The pH_2O/pCO_2 ratios are fixed and their values are presented in Table 3.

The fact that in the majority of the samples there is no trend in the $E_{a, app}$, by varying the pH_2/pCO_2 ratios, primarily shows that all samples, apart from the binary Au-modified, have similar intrinsic catalytic activity for the RWGS reaction. This is also concluded from the remark that the effect of the H_2 partial pressure on the CO production rate is almost linear. On the other hand, in the case of 3Au-Ni/GDC, there is an increase in $E_{a, app,}$ by increasing the pH_2/pCO_2 ratio. This is corroborated from the results in Figure 7, where r_{CO} seems to reach a plateau at high pH_2. The latter remarks indicate that the majority of the samples have actives sites that follow a similar reaction mechanism, in regards to the dissociative adsorption of H_2 and CO_2 towards the RWGS. On the other hand, the reaction mechanism seems to be different in the case of 3Au-Ni/GDC. In particular, it is implied that the high coverage of adsorbed H_2 may inhibit the CO_2 dissociative adsorption and thus decreases the intrinsic catalytic activity of the specific sample. This suggestion is going to be further clarified through the currently performed H_2O/CO_2 co-electrolysis measurements.

Carbon formation, through the Boudouard reaction (6), was also investigated and the results are presented in Figure 8. The slight scattering of the experimentally measured rates in combination with the theoretical values, where $r[CO_2]_{inlet}$ is equal to $r[CO + CO_2]_{outlet}$, suggest that there is no carbon deposition under the examined reaction conditions. This result is also in accordance with the fact that the Boudouard reaction is not thermodynamically favored above 750 °C [59].

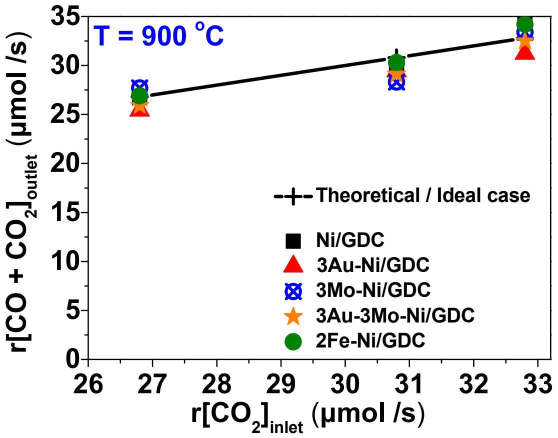

Figure 8. Investigation of the Boudouard reaction at 900 °C and 800 °C under OCP conditions on ESCs comprising: Ni/GDC, 3Au-Ni/GDC, 3Mo-Ni/GDC, 3Au–3Mo-Ni/GDC, and 2Fe-Ni/GDC. Theoretical case where $[CO_2]_{inlet}$ is equal to $[CO+CO_2]_{outlet}$ is also depicted with a solid line.

Previous studies [1,59,60] reported that at realistic CO_2/CO concentrations, during CO_2 electrolysis in the range of 650–750 °C, the equilibrium of (6) is shifted towards CO production (reaction (7)) and therefore carbon will not be formed, catalytically, during CO_2 electrolysis. In the case where the cell is operated at OCP conditions, as in our case, any coke deposited within the porous, modified or not, Ni/GDC electrode would be oxidized to CO according to the reverse Boudouard reaction (7) and thereby removed. Furthermore, the addition of steam in the feed is reported to remove carbon depositions according to reaction (8) [1,8]:

$$\text{Boudouard reaction:} \quad 2CO \rightarrow CO_2 + C \tag{7}$$

$$\text{Reverse Boudouard reaction:} \quad CO_2 + C \rightarrow 2CO \tag{8}$$

$$\text{Reaction of coke with } H_2O\text{:} \quad C + H_2O \rightarrow CO + H_2 \tag{9}$$

3. Materials and Methods

3.1. Preparation of Electrocatalysts

The modified cathode powders were prepared via the Deposition-Precipitation (D.P.) and Deposition-Co Precipitation (D.CP.) methods by using the commercial NiO/GDC cermet (65wt% NiO-35wt% GDC, Marion Technologies, Verniolle, France) as the support. The precursors for the 3wt% Au-NiO/GDC, 3wt% Mo-NiO/GDC, 3wt% Au−3wt% Mo-NiO/GDC, and 2wt% Fe-NiO/GDC samples were the $HAuCl_4$ (Sigma-Aldrich) or/and $(NH_4)_6Mo_7O_{24}$ (Sigma-Aldrich, St. Louis, MO, USA) and $Fe(NO_3)_3x9H_2O$ (Sigma-Aldrich, St. Louis, MO, USA) solutions, respectively. Full details about the synthesis can be found elsewhere [42,43]. After filtering, the precipitate was dried at 110 °C for 24 h. All dried powders were calcined at 600 °C/90 min and a part of them at 1100 °C/75 min. The first batch was used for the paste preparation, which is described in the following paragraph. The batch at 1100 °C was used for the physicochemical characterization. In this way, the prepared catalysts were studied at similar thermal stress as the calcined electrode-electrolyte assemblies.

3.2. Preparation of Electrolyte-Supported Half Cells

The electrolyte-supported half cells consisted of circular shaped planar 8YSZ electrolyte (by Kerafol) with a 25 mm diameter and 300 µm thickness. The fuel electrode was deposited by using the screen printing technique as reported in previous studies [23,46]. In particular, a paste was prepared by using an appropriate amount of the electrocatalyst (modified NiO/GDC powder), terpineol (Sigma-Aldrich, St. Louis, MO, USA) as the dispersant, and PVB (polyvinylbutyral, Sigma-Aldrich, St. Louis, MO, USA) as binder. After the deposition of the paste, the cell was sintered at 1150 °C with a heating/cooling ramp rate of 2 °C/min. The last temperature is the lowest possible in order to obtain proper adherence of the electrode on the electrolyte, whereas it is equivalent with the calcination temperature of the characterized powders (1100 °C). The examined electrodes were approximately 20 µm thick and their loading varied in the region of 10–12 mg/cm^2 with a 1.8 cm^2 geometric surface area (Figure 9). The prepared half cells were adjusted on a ceramic YSZ tube and sealed airtight with a glass sealing material manufactured by Kerafol.

(A)

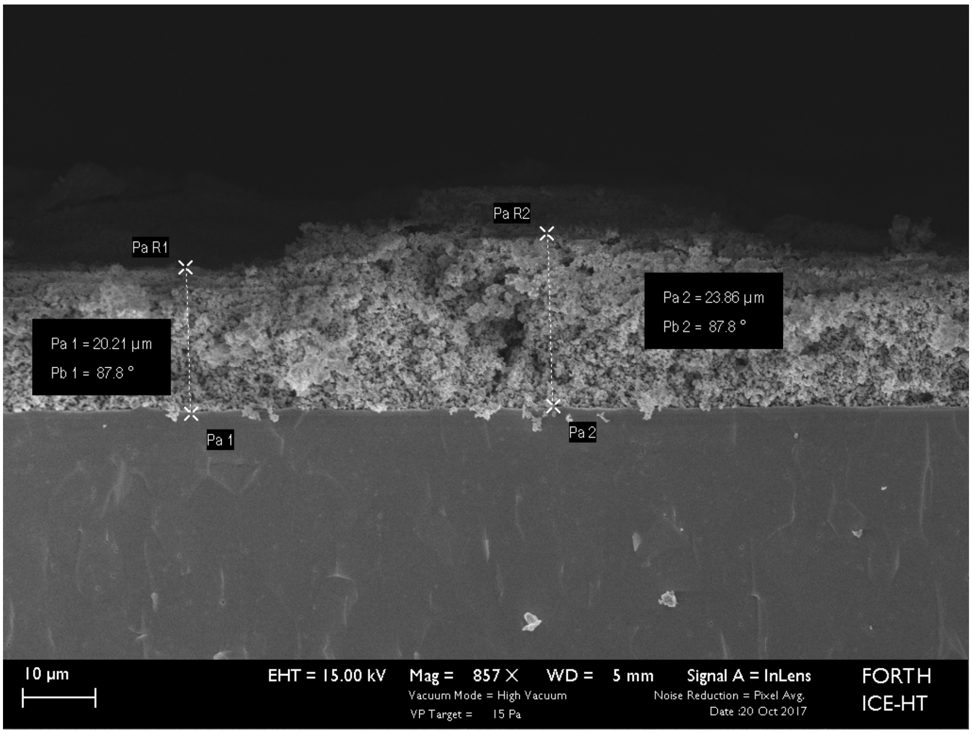

(**B**)

Figure 9. Images of a (half) electrolyte supported cell (ESC) prepared by screen printing: (**A**) NiO/GDC electrode and (**B**) SEM cross section perpendicular to the NiO/GDC//YSZ (half) electrolyte-supported cell.

3.3. Physicochemical Characterization

The samples, in the form of powders, were characterized with BET, H_2-TPR, Air-TPO, and TGA re-oxidation measurements in the presence of H_2O.

The BET specific surface area values of the samples were determined from the adsorption isotherms of nitrogen at −196 °C, recorded with a Micromeritics TriStar 3000 apparatus (Micromeritics, Norcross, GA, USA).

The re-oxidation measurements in the presence of H_2O, as well as H_2-TPR and Air-TPO measurements were carried out with a TA Q50 instrument. The H_2O re-oxidation properties of the powders were studied with TGA measurements, at a constant temperature in the range of 650–800 °C. Before the measurement, the samples were pre-reduced in-situ with 80 vol.% H_2/Ar at 800 °C for 100 min and then the feed was changed to 15.5 vol.% H_2O/Ar. The total flow rate (at STP conditions: 0 °C, 1 atm) was 100 cm^3/min and the loading of the measured samples was approximately 50 mg. Steam was introduced in the reactor by passing Ar through a saturator, which was maintained at a fixed temperature (65 °C).

3.4. Catalytic-Kinetic Measurements

The prepared half cells were catalytically investigated at Open Circuit Potential (OCP) conditions for the RWGS reaction, in the presence of Ni mesh. The catalytic experiments were accomplished at temperatures between 800–900 °C under various $H_2O/CO_2/H_2$ mixtures by keeping in all cases the P_{H_2O}/P_{CO_2} ratio constant. In regards to the experimental part of these measurements, H_2O was added and handled in the feed in the form of steam, as in the SOEC measurements. Before its evaporation, liquid H_2O was pressurized in a container and circulated in the system by means of a liquid water mass flow controller. Then, liquid H_2O was evaporated through lines and valves, heated at 160 °C, to prevent water condensation. The flow rate was fixed at 140 cm^3/min (at STP conditions: 0 °C, 1 atm), avoiding any mass transfer limitation effects in the reactor. Reactants and products were determined by using an on-line gas chromatograph (Varian CP-3800) with a thermal conductivity detector. Further details regarding the experimental parameters are indicated in the corresponding Figures.

4. Conclusions

The presented study deals with the kinetic investigation of Ni-based (modified or not) electrodes towards their performance for the RWGS reaction. The samples were examined in the form of electrolyte-supported (half) cells and the measured kinetic parameter was the production rate of CO. The main objective was to clarify the effect of the modification on the catalytic activity for the RWGS, which is considered as a key reaction for the CO production under H_2O/CO_2 co-electrolysis operation. The reaction conditions were similar to those that are applied under co-electrolysis mode.

Redox stability measurements in the presence of H_2O showed that the ternary 3Au–3Mo-Ni/GDC electrode is the least active sample for the dissociation of H_2O, having the highest $E_{a,app}$ and consequently the lowest binding energy for the H_2O_{ads}. On the other hand, the binary 2Fe-Ni/GDC is the most active sample for the dissociation of H_2O, thus having the potential to experience faster re-oxidation. Complementary characterization suggests that the interaction of Ni and Fe (FeO_x species in the oxidized form of the sample) during the H_2-reduction process increases the SSA_{BET} and affects the bulk properties of the binary Ni-Fe/GDC. The interaction can be realized through the possible formation of an Ni-Fe solid solution, which is currently under further clarification and may be responsible for enhancing the catalytic dissociation of H_2O_{ads}.

The kinetic study of the candidate electrocatalysts showed that Au modification inhibits the catalytic production of CO, through the RWGS reaction, while modification with Fe or Mo induces an enhancement of r_{CO}. In fact, the 2wt% Fe-Ni/GDC sample is the most active both in terms of %CO_2 conversion and of the produced CO. In addition, a negative synergy was observed for the ternary Au–Mo-Ni modified sample. Specifically, the 2wt% Fe-Ni/GDC and 3wt% Mo-Ni/GDC samples showed similar apparent activation energy for the RWGS reaction as that of Ni/GDC, while the 3wt% Au-Ni/GDC and 3wt% Au–3wt% Mo-Ni/GDC samples showed lower $E_{a,app}$. The above performance is observed for all applied fuel feeds (P_{H2}/P_{CO_2} = 0.86, 0.50, and 0.22), whereas it is enhanced by increasing (i) the operating temperature and (ii) the partial pressure of H_2.

Consequently, the kinetic behavior of all samples suggests that the production rate of CO exhibits a positive order dependence on the partial pressure of H_2, whereas carbon formation was not detected. In the case of the most active 2Fe-Ni/GDC sample, it is proposed that Fe-modification may enhance the catalytic dissociative adsorption of CO_2 towards the production of CO and this is further investigated. Finally, it is worth mentioning that the RWGS catalytic performance of both Fe- and Mo- modified samples is close to the equilibrium, but cannot be considered as thermodynamically limited.

Overall, the presented results correspond to a reference catalytic profile of the examined modified Ni/GDC samples for the RWGS reaction. These candidate electrocatalysts are currently being examined, as full electrolyte supported cells, in SOEC measurements for the H_2O/CO_2 co-electrolysis reaction to elucidate any additional effects by the applied current. Moreover, further investigation of the Fe-modification on NiO/GDC for the H_2O/CO_2 electrolysis processes will occur in the future.

Supplementary Materials: The following are available online at http://www.mdpi.com/2073-4344/9/2/151/s1, **Figure S1.** Kinetic study of the R.W.G.S. reaction on the nickel mesh (■), Ni/GDC with Ni mesh (●) and Ni/GDC without Ni mesh (△), in the range of 800–900 °C, under two different mixtures: (**A**) 24.5% H_2O − 24.5% CO_2 − 21% H_2 (P_{H2}/P_{CO_2} = 0.86) and (**B**) 28% H_2O − 28% CO_2 − 14% H_2 (P_{H2}/P_{CO_2} = 0.50). Dilution of He: 30 vol.% and F_{total} = 140 cm^3/min (at STP conditions: 0 °C, 1 atm) in all cases. The loading of Ni/GDC is 11 mg/cm^2.

Author Contributions: Conceptualization, S.N. and D.N.; Data curation, E.I.; Formal analysis, E.I.; Funding acquisition, S.N. and D.N.; Investigation, E.I.; Methodology, S.N. and D.N.; Supervision, S.N. and D.N.; Validation, S.N. and D.N.; Writing—original draft, D.N.; Writing—review & editing, S.N., D.N. and E.I.

Funding: The research leading to these results has received funding from the Fuel Cells and Hydrogen 2 Joint Undertaking under the project SElySOs with Grant Agreement No: 671481. This Joint Undertaking receives support from the European Union's Horizon 2020 Research and Innovation Programme and Greece, Germany, Czech Republic, France, and Norway.

Conflicts of Interest: The authors declare no conflict of interest.

References

1. Ebbesen, S.D.; Mogensen, M. Electrolysis of carbon dioxide in Solid Oxide Electrolysis Cells. *J. Power Sources* **2009**, *193*, 349–358. [CrossRef]
2. Graves, C.; Ebbesen, S.D.; Mogensen, M.; Lackner, K.S. Sustainable hydrocarbon fuels by recycling CO_2 and H_2O with renewable or nuclear energy. *Renew. Sustain. Energy Rev.* **2011**, *15*, 1–23. [CrossRef]
3. Tao, Y.; Ebbesen, S.D.; Mogensen, M.B. Carbon Deposition in Solid Oxide Cells during Co-Electrolysis of H_2O and CO_2. *J. Electrochem. Soc.* **2014**, *161*, F337–F343. [CrossRef]
4. Moçoteguy, P.; Brisse, A. A review and comprehensive analysis of degradation mechanisms of solid oxide electrolysis cells. *Int. J. Hydrogen Energy* **2013**, *38*, 15887–15902. [CrossRef]
5. Laguna-Bercero, M.A. Recent advances in high temperature electrolysis using solid oxide fuel cells: A review. *J. Power Sources* **2012**, *203*, 4–16. [CrossRef]
6. Petipas, F.; Brisse, A.; Bouallou, C. Benefits of external heat sources for high temperature electrolyser systems. *Int. J. Hydrogen Energy* **2014**, *39*, 5505–5513. [CrossRef]
7. Zhang, X.; Song, Y.; Wang, G.; Bao, X. Co-electrolysis of CO_2 and H_2O in high-temperature solid oxide electrolysis cells: Recent advance in cathodes. *J. Energy Chem.* **2017**, *26*, 839–853. [CrossRef]
8. Sun, X.; Chen, M.; Jensen, S.H.; Ebbesen, S.D.; Graves, C.; Mogensen, M. Thermodynamic analysis of synthetic hydrocarbon fuel production in pressurized solid oxide electrolysis cells. *Int. J. Hydrogen Energy* **2012**, *37*, 17101–17110. [CrossRef]
9. Kim, S.-W.; Kim, H.; Yoon, K.J.; Lee, J.-H.; Kim, B.-K.; Choi, W.; Lee, J.-H.; Hong, J. Reactions and mass transport in high temperature co-electrolysis of steam/CO_2 mixtures for syngas production. *J. Power Sources* **2015**, *280*, 630–639. [CrossRef]
10. Li, W.; Wang, H.; Shi, Y.; Cai, N. Performance and methane production characteristics of H_2O–CO_2 co-electrolysis in solid oxide electrolysis cells. *Int. J. Hydrogen Energy* **2013**, *38*, 11104–11109. [CrossRef]

11. Mahmood, A.; Bano, S.; Yu, J.H.; Lee, K.-H. Effect of operating conditions on the performance of solid electrolyte membrane reactor for steam and CO_2 electrolysis. *J. Membr. Sci.* **2015**, *473*, 8–15. [CrossRef]
12. Sun, X.; Chen, M.; Liu, Y.-L.; Hjalmarsson, P.; Ebbesen, S.D.; Jensen, S.H.; Mogensen, M.B.; Hendriksen, P.V. Durability of Solid Oxide Electrolysis Cells for Syngas Production. *J. Electrochem. Soc.* **2013**, *160*, F1074–F1080. [CrossRef]
13. Ebbesen, S.D.; Graves, C.; Mogensen, M. Production of Synthetic Fuels by Co-Electrolysis of Steam and Carbon Dioxide. *Int. J. Green Energy* **2009**, *6*, 646–660. [CrossRef]
14. Graves, C.; Ebbesen, S.D.; Mogensen, M. Co-electrolysis of CO_2 and H_2O in solid oxide cells: Performance and durability. *Solid State Ion.* **2011**, *192*, 398–403. [CrossRef]
15. Diethelm, S.; Herle, J.V.; Montinaro, D.; Bucheli, O. Electrolysis and Co-Electrolysis Performance of SOE Short Stacks. *Fuel Cells* **2013**, *13*, 631–637. [CrossRef]
16. Kim-Lohsoontorn, P.; Bae, J. Electrochemical performance of solid oxide electrolysis cell electrodes under high-temperature coelectrolysis of steam and carbon dioxide. *J. Power Sources* **2011**, *196*, 7161–7168. [CrossRef]
17. Stoots, C.; O'Brien, J.; Hartvigsen, J. Results of recent high temperature coelectrolysis studies at the Idaho National Laboratory. *Int. J. Hydrogen Energy* **2009**, *34*, 4208–4215. [CrossRef]
18. Ni, M. 2D thermal modeling of a solid oxide electrolyzer cell (SOEC) for syngas production by H_2O/CO_2 co-electrolysis. *Int. J. Hydrogen Energy* **2012**, *37*, 6389–6399. [CrossRef]
19. Ni, M. An electrochemical model for syngas production by co-electrolysis of H_2O and CO_2. *J. Power Sources* **2012**, *202*, 209–216. [CrossRef]
20. Yue, X.; Irvine, J.T.S. (La,Sr)(Cr,Mn)O_3/GDC cathode for high temperature steam electrolysis and steam-carbon dioxide co-electrolysis. *Solid State Ion.* **2012**, *225*, 131–135. [CrossRef]
21. Zhan, Z.; Zhao, L. Electrochemical reduction of CO_2 in solid oxide electrolysis cells. *J. Power Sources* **2010**, *195*, 7250–7254. [CrossRef]
22. Ebbesen, S.D.; Jensen, S.H.; Hauch, A.; Mogensen, M.B. High Temperature Electrolysis in Alkaline Cells, Solid Proton Conducting Cells, and Solid Oxide Cells. *Chem. Rev.* **2014**, *114*, 10697–10734. [CrossRef]
23. Neofytidis, C.; Dracopoulos, V.; Neophytides, S.G.; Niakolas, D.K. Electrocatalytic performance and carbon tolerance of ternary Au-Mo-Ni/GDC SOFC anodes under CH_4-rich Internal Steam Reforming conditions. *Catal. Today* **2018**, *310*, 157–165. [CrossRef]
24. Liang, M.; Yu, B.; Wen, M.; Chen, J.; Xu, J.; Zhai, Y. Preparation of NiO–YSZ composite powder by a combustion method and its application for cathode of SOEC. *Int. J. Hydrogen Energy* **2010**, *35*, 2852–2857. [CrossRef]
25. Kleiminger, L.; Li, T.; Li, K.; Kelsall, G.H. CO_2 splitting into CO and O_2 in micro-tubular solid oxide electrolysers. *RSC Adv.* **2014**, *4*, 50003–50016. [CrossRef]
26. Marina, O.A.; Pederson, L.R.; Williams, M.C.; Coffey, G.W.; Meinhardt, K.D.; Nguyen, C.D.; Thomsen, E.C. Electrode Performance in Reversible Solid Oxide Fuel Cells. *J. Electrochem. Soc.* **2007**, *154*, B452–B459. [CrossRef]
27. Hjalmarsson, P.; Sun, X.; Liu, Y.-L.; Chen, M. Durability of high performance Ni–yttria stabilized zirconia supported solid oxide electrolysis cells at high current density. *J. Power Sources* **2014**, *262*, 316–322. [CrossRef]
28. Tao, Y.; Ebbesen, S.D.; Mogensen, M.B. Degradation of solid oxide cells during co-electrolysis of steam and carbon dioxide at high current densities. *J. Power Sources* **2016**, *328*, 452–462. [CrossRef]
29. Hauch, A.; Ebbesen, S.D.; Jensen, S.H.; Mogensen, M. Solid Oxide Electrolysis Cells: Microstructure and Degradation of the Ni/Yttria-Stabilized Zirconia Electrode. *J. Electrochem. Soc.* **2008**, *155*, B1184–B1193. [CrossRef]
30. Chen, M.; Liu, Y.-L.; Bentzen, J.J.; Zhang, W.; Sun, X.; Hauch, A.; Tao, Y.; Bowen, J.R.; Hendriksen, P.V. Microstructural Degradation of Ni/YSZ Electrodes in Solid Oxide Electrolysis Cells under High Current. *J. Electrochem. Soc.* **2013**, *160*, F883–F891. [CrossRef]
31. Tietz, F.; Sebold, D.; Brisse, A.; Schefold, J. Degradation phenomena in a solid oxide electrolysis cell after 9000 h of operation. *J. Power Sources* **2013**, *223*, 129–135. [CrossRef]
32. Knibbe, R.; Traulsen, M.L.; Hauch, A.; Ebbesen, S.D.; Mogensen, M. Solid Oxide Electrolysis Cells: Degradation at High Current Densities. *J. Electrochem. Soc.* **2010**, *157*, B1209–B1217. [CrossRef]
33. Hauch, A.; Brodersen, K.; Chen, M.; Mogensen, M.B. Ni/YSZ electrodes structures optimized for increased electrolysis performance and durability. *Solid State Ion.* **2016**, *293*, 27–36. [CrossRef]

34. Papaefthimiou, V.; Niakolas, D.K.; Paloukis, F.; Teschner, D.; Knop-Gericke, A.; Haevecker, M.; Zafeiratos, S. Operando observation of nickel/ceria electrode surfaces during intermediate temperature steam electrolysis. *J. Catal.* **2017**, *352*, 305–313. [CrossRef]
35. Liu, S.; Chuang, K.T.; Luo, J.-L. Double-Layered Perovskite Anode with in Situ Exsolution of a Co–Fe Alloy To Cogenerate Ethylene and Electricity in a Proton-Conducting Ethane Fuel Cell. *ACS Catal.* **2016**, *6*, 760–768. [CrossRef]
36. Nishida, R.; Puengjinda, P.; Nishino, H.; Kakinuma, K.; Brito, M.E.; Watanabe, M.; Uchida, H. High-performance electrodes for reversible solid oxide fuel cell/solid oxide electrolysis cell: Ni-Co dispersed ceria hydrogen electrodes. *RSC Adv.* **2014**, *4*, 16260–16266. [CrossRef]
37. Kim, S.-W.; Park, M.; Kim, H.; Yoon, K.J.; Son, J.-W.; Lee, J.-H.; Kim, B.-K.; Lee, J.-H.; Hong, J. Catalytic Effect of Pd-Ni Bimetallic Catalysts on High-Temperature Co-Electrolysis of Steam/CO_2 Mixtures. *J. Electrochem. Soc.* **2016**, *163*, F3171–F3178. [CrossRef]
38. Ishihara, T.; Jirathiwathanakul, N.; Zhong, H. Intermediate temperature solid oxide electrolysis cell using $LaGaO_3$ based perovskite electrolyte. *Energy Environ. Sci.* **2010**, *3*, 665–672. [CrossRef]
39. Wang, S.; Inoishi, A.; Hong, J.-E.; Ju, Y.-W.; Hagiwara, H.; Ida, S.; Ishihara, T. Ni–Fe bimetallic cathodes for intermediate temperature CO_2 electrolyzers using a La0.9Sr0.1Ga0.8Mg0.2O_3 electrolyte. *J. Mater. Chem. A* **2013**, *1*, 12455–12461. [CrossRef]
40. Back, S.; Jung, Y. Importance of Ligand Effects Breaking the Scaling Relation for Core–Shell Oxygen Reduction Catalysts. *ChemCatChem* **2017**, *9*, 3173–3179. [CrossRef]
41. Cho, A.; Ko, J.; Kim, B.-K.; Han, J.W. Electrocatalysts with Increased Activity for Coelectrolysis of Steam and Carbon Dioxide in Solid Oxide Electrolyzer Cells. *ACS Catal.* **2018**, 967–976. [CrossRef]
42. Niakolas, D.K.; Athanasiou, M.; Dracopoulos, V.; Tsiaoussis, I.; Bebelis, S.; Neophytides, S.G. Study of the synergistic interaction between nickel, gold and molybdenum in novel modified NiO/GDC cermets, possible anode materials for CH_4 fueled SOFCs. *Appl. Catal. A Gen.* **2013**, *456*, 223–232. [CrossRef]
43. Niakolas, D.K.; Ouweltjes, J.P.; Rietveld, G.; Dracopoulos, V.; Neophytides, S.G. Au-doped Ni/GDC as a new anode for SOFCs operating under rich CH_4 internal steam reforming. *Int. J. Hydrogen Energy* **2010**, *35*, 7898–7904. [CrossRef]
44. Neofytidis, C.; Athanasiou, M.; Neophytides, S.G.; Niakolas, D.K. Sulfur Tolerance of Au–Mo–Ni/GDC SOFC Anodes Under Various CH_4 Internal Steam Reforming Conditions. *Top. Catal.* **2015**, *58*, 1276–1289. [CrossRef]
45. Niakolas, D.K.; Neofytidis, C.S.; Neophytides, S.G. Effect of Au and/or Mo Doping on the Development of Carbon and Sulfur Tolerant Anodes for SOFCs—A Short Review. *Front. Environ. Sci.* **2017**, *5*. [CrossRef]
46. Ioannidou, E.; Neofytidis, C.; Sygellou, L.; Niakolas, D.K. Au-doped Ni/GDC as an Improved Cathode Electrocatalyst for H_2O Electrolysis in SOECs. *Appl. Catal. B Environ.* **2018**, *236*, 253–264. [CrossRef]
47. Wandekar, R.V.; Ali, M.; Wani, B.N.; Bharadwaj, S.R. Physicochemical studies of NiO–GDC composites. *Mater. Chem. Phys.* **2006**, *99*, 289–294. [CrossRef]
48. Sarantaridis, D.; Atkinson, A. Redox Cycling of Ni-Based Solid Oxide Fuel Cell Anodes: A Review. *Fuel Cells* **2007**, *7*, 246–258. [CrossRef]
49. Ettler, M.; Timmermann, H.; Malzbender, J.; Weber, A.; Menzler, N.H. Durability of Ni anodes during reoxidation cycles. *J. Power Sources* **2010**, *195*, 5452–5467. [CrossRef]
50. Atkinson, A.; Smart, D.W. Transport of Nickel and Oxygen during the Oxidation of Nickel and Dilute Nickel/Chromium Alloy. *J. Electrochem. Soc.* **1988**, *135*, 2886–2893. [CrossRef]
51. Ghosh, S.; Hariharan, S.; Tiwari, A.K. Water Adsorption and Dissociation on Copper/Nickel Bimetallic Surface Alloys: Effect of Surface Temperature on Reactivity. *J. Phys. Chem. C* **2017**, *121*, 16351–16365. [CrossRef]
52. Gan, L.-Y.; Tian, R.-Y.; Yang, X.-B.; Lu, H.-D.; Zhao, Y.-J. Catalytic Reactivity of CuNi Alloys toward H_2O and CO Dissociation for an Efficient Water–Gas Shift: A DFT Study. *J. Phys. Chem. C* **2012**, *116*, 745–752. [CrossRef]
53. Gu, X.-K.; Nikolla, E. Fundamental Insights into High-Temperature Water Electrolysis Using Ni-Based Electrocatalysts. *J. Phys. Chem. C* **2015**, *119*, 26980–26988. [CrossRef]
54. Niakolas, D.K. Sulfur poisoning of Ni-based anodes for Solid Oxide Fuel Cells in H/C-based fuels. *Appl. Catal. A Gen.* **2014**, *486*, 123–142. [CrossRef]

55. Sapountzi, F.M.; Zhao, C.; Boreave, A.; Retailleau-Mevel, L.; Niakolas, D.; Neofytidis, C.; Vernoux, P. Sulphur tolerance of Au-modified Ni/GDC during catalytic methane steam reforming. *Catal. Sci. Technol.* **2018**, *8*, 1578–1588. [CrossRef]
56. Besenbacher, F.; Chorkendorff, I.; Clausen, B.S.; Hammer, B.; Molenbroek, A.M.; Norskov, J.K.; Stensgaard, I. Design of a surface alloy catalyst for steam reforming. *Science* **1998**, *279*, 1913–1915. [CrossRef]
57. Water-Gas Shift Reaction. Available online: https://en.wikipedia.org/wiki/Water-gas_shift_reaction (accessed on 10 December 2018).
58. Caitlin, C. *Kinetics and Catalysis of the Water-Gas-Shift Reaction: A Microkinetic and Graph Theoretic Approach*; Worcester Polytechnic Institute: Worcester, MA, USA, 2006.
59. Stoots, C.M.; O'Brien, J.E.; Herring, J.S.; Hartvigsen, J.J. Syngas Production via High-Temperature Coelectrolysis of Steam and Carbon Dioxide. *J. Fuel Cell Sci. Technol.* **2008**, *6*. [CrossRef]
60. Sasaki, K.; Teraoka, Y. Equilibria in Fuel Cell Gases: II. The C-H-O Ternary Diagrams. *J. Electrochem. Soc.* **2003**, *150*, A885–A888. [CrossRef]